Overcoming the strength-ductility trade-off in refractory medium-entropy alloys via controlled B2 ordering

N. Yurchenko, E. Panina, A. Tojibaev, S. Zherebtsov & N. Stepanov

MATERIALS RESEARCH LETTERS

Taylor & Francis
Taylor & Francis Group

ORIGINAL REPORTS

🔓 OPEN ACCESS   Check for updates

Overcoming the strength-ductility trade-off in refractory medium-entropy alloys via controlled B2 ordering

N. Yurchenko ⓘ, E. Panina ⓘ, A. Tojibaev, S. Zherebtsov ⓘ and N. Stepanov ⓘ

Laboratory of Bulk Nanostructured Materials, Belgorod National Research University, Belgorod, Russia

ABSTRACT

Herein, we showed that controlled additions of Al, which provided a certain degree of B2 ordering, resulted in a $\sim$ 37%-enhancement of both yield strength and uniform elongation in $Al_x(NbTiZr)_{100-x}$ ($x = 0$; 2.5; 5; 7.5 at.%) refractory medium-entropy alloys. The improvement of properties stemmed from the solid solution and short-range order strengthening, as well as from the alteration in a character of dislocation glide. The B2 ordering caused the formation of multiple dislocation bands and the activation of cross-slip, which improved the macroscopic stability of plastic flow and extended the strengthening stage, thereby postponing necking.
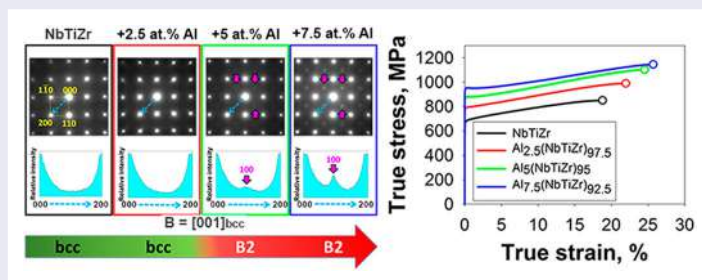
IMPACT STATEMENT

Controlled Al-induced B2 ordering helps overcome the strength-ductility dilemma in refractory medium-entropy alloys due to solid solution and short-range strengthening coupled with the dislocation motion changing.

Introduction

Chemical ordering in body-centred cubic (bcc) refractory high/medium-entropy alloys (RH/MEAs), designed for high-temperature service [1–4], has been gained particular attention among the researchers in recent years [4–40]. Great interest in such a phenomenon is because of its crucial effect on the mechanical properties. Specifically, many Al-containing RH/MEAs, in which Al induced the formation of a B2 (ordered bcc) structure, possessed higher strength at 22-1350°C compared to Al-free counterparts [2,11,30,33,36,38]. Some of these alloys showed yield strength anomaly [24,37], i.e. became stronger with the temperature rise. Meantime, a large part of B2-ordered RH/MEAs had limited plasticity at ambient or intermediate temperatures [7,9,11,19,30,33,37].

To date, several efforts have been made to balance the mechanical performance of B2-ordered RH/MEAs [7,10,19]. However, even a slight increase in the plasticity of B2-ordered RH/MEAs, provided by either chemical (elimination/decrease in the degree of B2 ordering [7,19]) or microstructure (the B2 matrix-to-B2 particles transition [10]) engineering, has resulted in a notable strength degradation. More importantly, the room-temperature tensile ductility, required for potential applications of these alloys as structural materials [41], remained unreported or unachievable.

In the current study, we, for the first time, showed that the enlargement of the degree of B2 ordering in a controllable fashion could overcome the strength-ductility trade-off in RH/MEAs. This counterintuitive strategy was

tested on a model bcc NbTiZr RMEA having decent tensile ductility and medium strength [42,43], which was alloyed with various amounts of Al to invoke the B2 ordering. Our results demonstrated that the B2 ordering was a more effective way to improve the overall mechanical performance of the NbTiZr alloy compared to the already reported approaches [44,45].

Materials and methods

The alloys with nominal compositions of NbTiZr, $Al_{2.5}(NbTiZr)_{97.5}$, $Al_5(NbTiZr)_{95}$, and $Al_{7.5}(NbTiZr)_{92.5}$ (at.%) were produced by the vacuum arc melting of pure metals. The as-cast ingots were cold rolled to a thickness strain of 80%, sealed in vacuumed (10^{-2} torr) quartz tubes, annealed at 900°C for 0.5 h, and water quenched. Tensile specimens with the gauge dimensions of $6 \times 3 \times 1\,mm^3$ were cut from the annealed sheets. Tensile tests were performed at room temperature in a laboratory air at a constant strain rate of $10^{-3}\ s^{-1}$ (Instron 5882). The digital image correlation (DIC) technique was employed to visualise the distribution of local strains produced during the tensile tests. The in-plane Lagrangian strains were measured using a commercial Vic-3D™ system (Correlated Solutions, Inc).

Microstructural investigations were performed using X-ray diffraction (XRD; RIGAKU diffractometer and Cu Kα radiation), electron backscatter diffraction (EBSD; FEI Quanta 600 FEG), and transmission electron microscopy (TEM; JEM JEOL-2100). Selected area diffraction patterns (SADPs) were collected in a $<001>_{bcc}$ zone axis at an exposure time of 16 s. Intensity line profiles along the g_{200} vector and the threshold segmentation were constructed using an ImageJ software. Dark-field images taken from the aperture positions corresponded to a half-length of the g_{200} vector were acquired at an exposure time of 32 s.

Results and discussion

Figure 1 collects the data on microstructure and phase composition of the $Al_x(NbTiZr)_{100-x}$ alloys. The actual chemical compositions of the alloys are given in Table S1 (Supplementary material). EBSD analysis revealed a fully recrystallised microstructure in all the alloys (Figures 1(a-d)). Average grain sizes were close to $\sim 20\ \mu$m; however, small deviations from this mean value should be noted (Figure S1, Supplementary material). An initial evaluation by XRD showed that the alloys had a single-phase bcc structure (Figure S2, Supplementary material). TEM investigation, based on the assessment of SADPs taken in $<001>_{bcc}$ zone axes and the intensity line

profiles along the g_{200} vector (which showed no local maxima at their half-lengths), confirmed the bcc structure in the NbTiZr and $Al_{2.5}(NbTiZr)_{97.5}$ alloys (Figures 1(e, f, i, j)). Meanwhile, we detected diffuse and faint 100 B2 superlattice spots in the $Al_5(NbTiZr)_{95}$ alloy (denoted with pink arrows in Figure 1(g)). These B2 superlattice spots were sharper and brighter in the $Al_{7.5}(NbTiZr)_{92.5}$ alloy (Figure 1(h)). The intensity line profiles along the g_{200} vector disclosed approximately four times higher local maxima corresponding to their half-lengths, i.e. the 100 positions, in the $Al_{7.5}(NbTiZr)_{92.5}$ alloy compared to those in the $Al_5(NbTiZr)_{95}$ alloy (Figures 1(k, l)).

Data obtained in the current study confirmed limited applicability of XRD analysis for revealing of the B2 ordering in (R)H/MEAs with low Al contents [17,46–48]. Only by TEM analysis, we discovered the smallest (> 2.6 at.%) threshold Al concentration for the bcc-to-B2 transition, recorded to date for RH/MEAs [19,22,30], lightweight H/MEAs (LWH/MEAs) [49,50], and beta-Ti alloys [51]. Besides, an examination of SADPs via the intensity profile lines could give us a semi-quantitive appraisal of a degree of ordering in the $Al_x(NbTiZr)_{100-x}$ alloys. Through comparison of the relative intensities of superlattice and fundamental spots [52–57], albeit without counting the scattering factors, we established that the Al additions from 5.3–7.7 at.% increased the degree of B2 ordering by about four times.

Here, the term 'degree of B2 ordering' must be clarified. In previous works [7,8,14,19], a multi-component B2 matrix phase in Al-containing RH/MEAs was assumed as a continuous entity with an imperfect lattice containing atoms of constitutive elements, arranged both in random (bcc) and preferential (B2) positions. The occupancy of the B2 sites by a certain sort of atoms, mostly by Al ones, characterised the degree of B2 ordering, which could vary from 0 (disordered) to 1 (ordered), similarly to binary alloys [58]. Meantime, Qiao et al. [30] recently revealed a diffusionless transfer from short- to long-range B2 ordered domains with an increase in the Al content. In that case, the degree of B2 ordering was considered as a dimensional parameter instead of the site occupancy factor.

To gain insight into the B2 ordering phenomenon in the $Al_x(NbTiZr)_{100-x}$ alloys, we performed a more detailed TEM study (Figure 2). Dark-field imaging of the NbTiZr and $Al_{7.5}(NbTiZr)_{92.5}$ alloys under prolonged exposure at the aperture position corresponded to the half-length of the g_{200} vector (which, in the case of the $Al_{7.5}(NbTiZr)_{92.5}$ alloy, was conformed to the (100) superlattice spot) revealed a clear difference in their fine microstructures (Figure 2). No contrast was observed in the NbTiZr alloy (Figure 2(a)), while, in the $Al_{7.5}(NbTiZr)_{92.5}$ alloy, profuse bright B2 domains
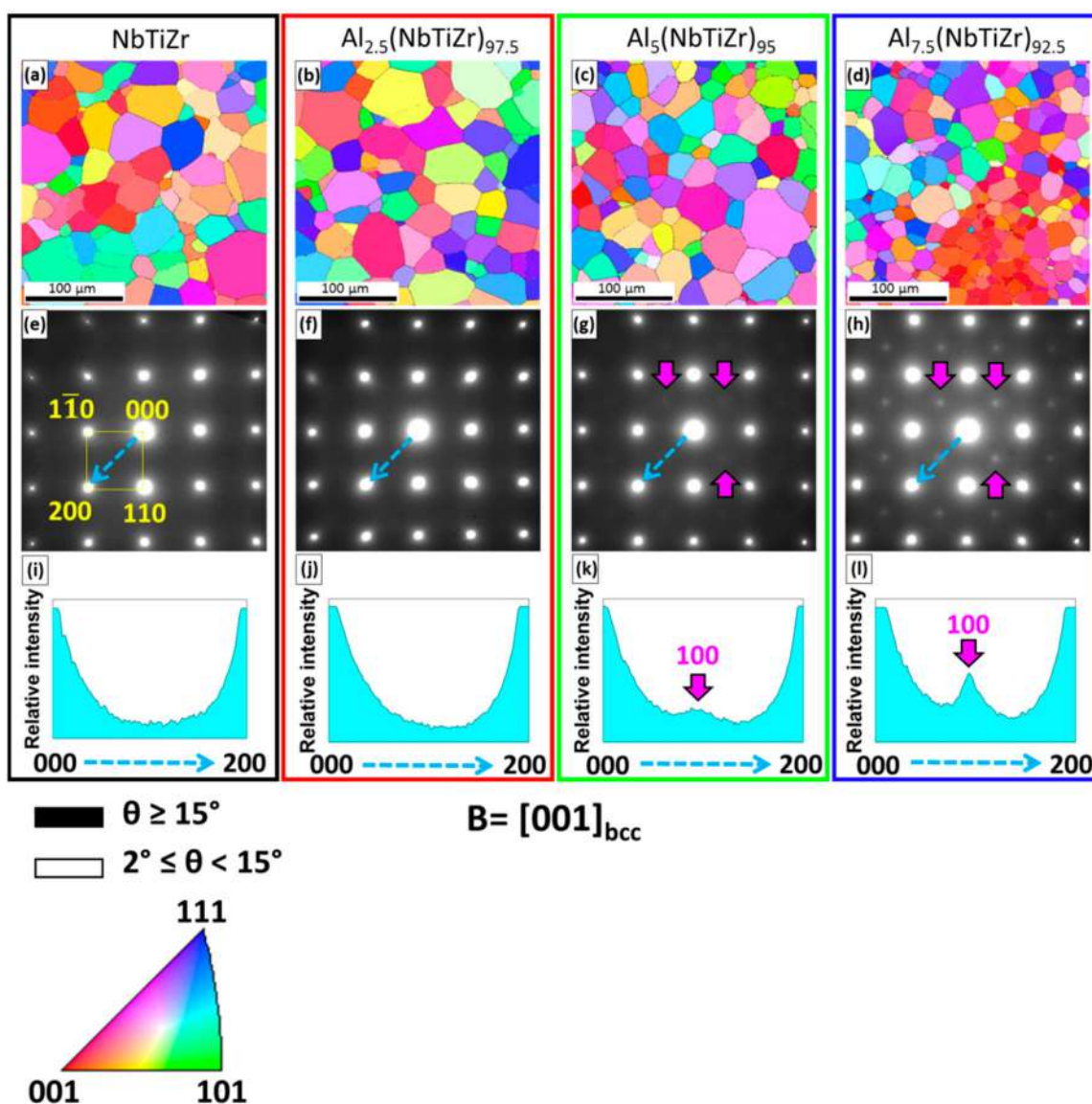
Figure 1. Characterisation of microstructure and phase composition of the $Al_x(NbTiZr)_{100-x}$ alloys: (a-d) – inverse pole figures (IPF), showing the fully recrystallised microstructure of the NbTiZr (a), $Al_{2.5}(NbTiZr)_{97.5}$ (b), $Al_5(NbTiZr)_{95}$ (c), and $Al_{7.5}(NbTiZr)_{92.5}$ (d) alloys; (e-h) – SADPs, acquired in $[001]_{bcc}$ zone axes of the NbTiZr (e), $Al_{2.5}(NbTiZr)_{97.5}$ (f), $Al_5(NbTiZr)_{95}$ (g), and $Al_{7.5}(NbTiZr)_{92.5}$ (h) alloys. Pink arrows in Figures 1(g, h) highlighted the 100_{B2} superlattice spots in the $Al_5(NbTiZr)_{95}$ (g) and $Al_{7.5}(NbTiZr)_{92.5}$ (h) alloys; (i-l) – intensity line profiles along the g_{200} vectors (the directions are denoted with dashed blue arrows in SADPs Figures 1(e-h)) for the NbTiZr (i), $Al_{2.5}(NbTiZr)_{97.5}$ (j), $Al_5(NbTiZr)_{95}$ (g), and $Al_{7.5}(NbTiZr)_{92.5}$ (h) alloys. Pink arrows in Figures 1(k, l) denoted the peaks, corresponded to the 100 local maxima in the $Al_5(NbTiZr)_{95}$ (k) and $Al_{7.5}(NbTiZr)_{92.5}$ (l) alloys.

could be distinguished (Figure 2(b)). The threshold segmentation (Figures 2(c, d)) suggested the average size, $\bar{d}$, standard deviation, σ, and fraction, f, of these B2 domains as 0.82, 0.33 nm, and $\sim$ 20%, respectively (Figure 2(e)). The dimensions of $<$ 1 nm allowed identifying these B2 domains as short-range ordered (SRO) entities [54,59,60].

Based on the domain ordering mechanism proposed by Qiao et al. [30], the following scheme of the B2 ordering in the $Al_x(NbTiZr)_{100-x}$ alloys could be suggested.

The Al additions first provoked the bcc-to-B2 transition (between the $Al_{2.5}(NbTiZr)_{97.5}$ and $Al_5(NbTiZr)_{95}$ alloys), i.e. resulted in the formation of the B2 SRO domains with a very small size, and then increased the degree of B2 ordering (between the $Al_5(NbTiZr)_{95}$ and $Al_{7.5}(NbTiZr)_{92.5}$ alloys) due to growing of these B2 SRO domains. However, further in-depth investigations are needed to elucidate peculiarities of the B2 ordering more thoroughly, which are beyond the limit of the current paper.
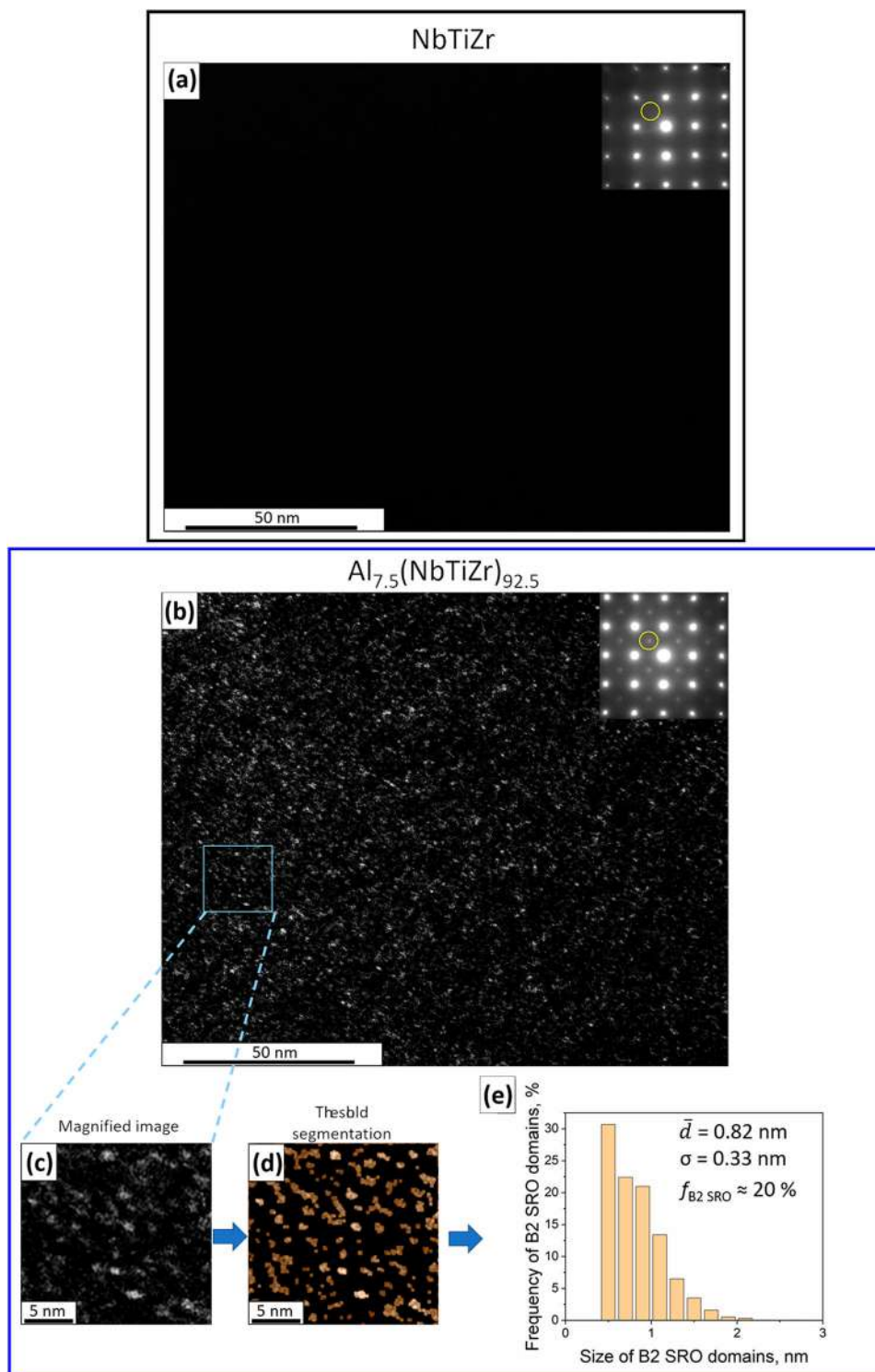
Figure 2. Detailed characterisation of the fine structure of the NbTiZr and $Al_{7.5}(NbTiZr)_{92.5}$ alloys: (a, b) – typical dark-field TEM images taken from the aperture position marked with yellow circles (corresponded to the half-length of the g_{200} vector in SADP of each alloy), showing the absence of any contrast in the NbTiZr (a) alloy and profuse B2 domains in the $Al_{7.5}(NbTiZr)_{92.5}$ (b) alloy; (c, d) – typical magnified dark-field images before (b) and after (c) the threshold segmentation procedure; (e) – histogram, illustrating the size distribution of the B2 SRO domains with the estimated values of average size, $\bar{d}$, standard deviation, σ, and fraction, f.
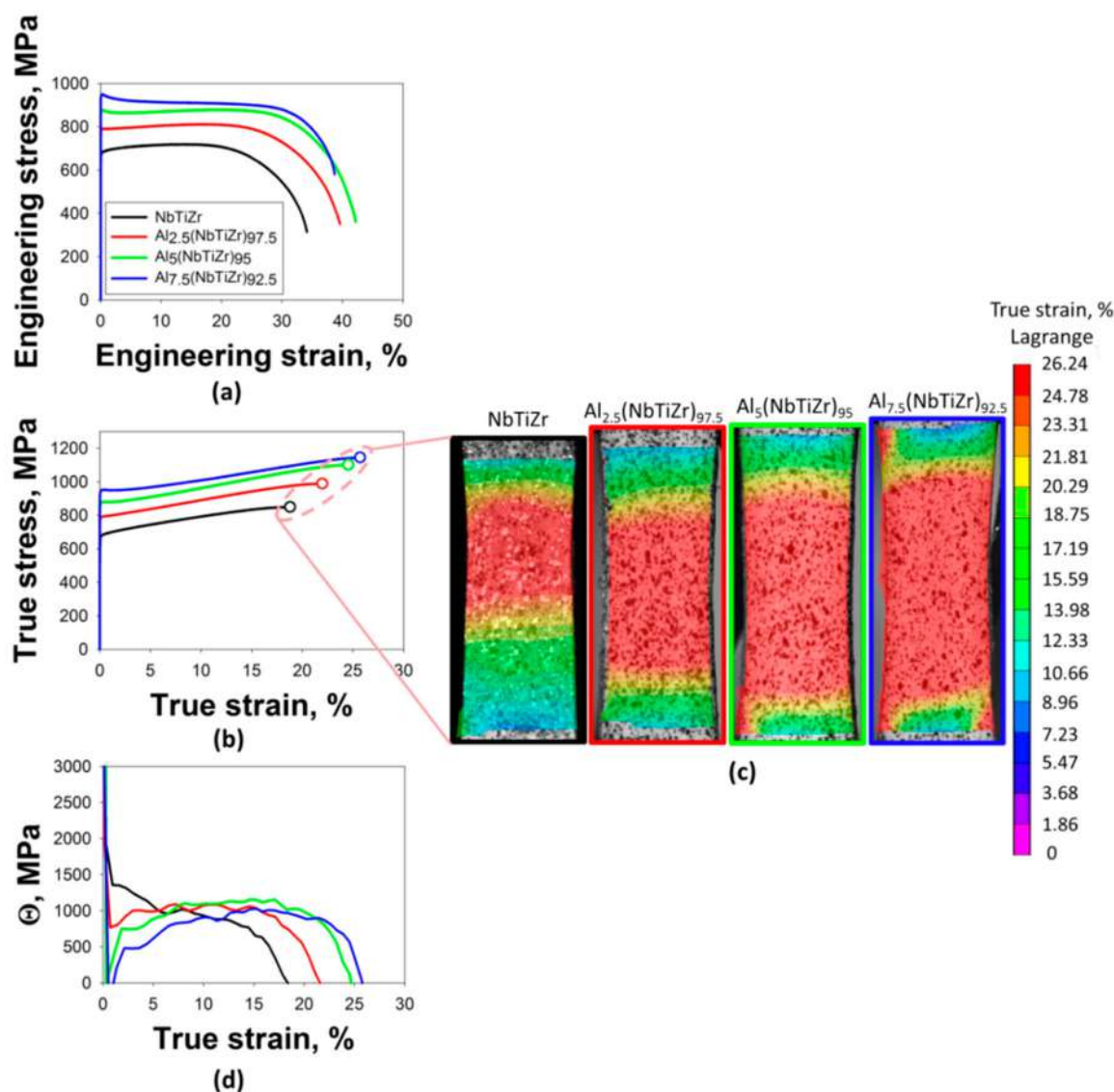
Figure 3. Characterisation of room-temperature tensile mechanical properties of the $Al_x(NbTiZr)_{100-x}$ alloys: (a) – engineering stress-strain curves; (b) – true stress-strain curves; (c) – DIC images of tensile specimens, taken at the necking formation and demonstrating the strain distribution along the cross-section; (d) – evolution of strain hardening rate, θ, with the strain.

Table 1. Yield strength, YS, ultimate tensile strength, UTS, uniform elongation, UE, elongation to fracture, EF, and apparent activation volume, V∗, obtained during room-temperature tensile and stress relaxation tests of the $Al_x(NbTiZr)_{100-x}$ alloys.

Alloy	YS, MPa	UTS, MPa	UE, %	EF, %	V∗, b³
NbTiZr	680 ± 5	715 ± 10	18.8 ± 0.6	34.1 ± 0.8	∼ 70–60
$Al_{2.5}(NbTiZr)_{97.5}$	785 ± 5	810 ± 5	22.0 ± 0.8	39.6 ± 0.7	∼ 67–59
$Al_5(NbTiZr)_{95}$	845 ± 40	860 ± 30	24.5 ± 0.4	42.2 ± 0.5	∼ 49–61
$Al_{7.5}(NbTiZr)_{92.5}$	930 ± 20	935 ± 20	25.7 ± 2.3	38.7 ± 2.0	∼ 50–68

Note: For V∗, a range of values, evolving with the strain, are given.

Figure 3 and Table 1 represent the tensile mechanical properties of the $Al_x(NbTiZr)_{100-x}$ alloys.

The Al additions increased yield strength, *YS*, from 680 MPa in the NbTiZr alloy to 930 MPa in the $Al_{7.5}(NbTiZr)_{92.5}$ alloy (Figure 3(a); Table 1). According to the engineering stress–strain curves, after yielding, the Al-containing alloys experienced a short strengthening stage followed first by a stress reduction, then continuous yielding, which extended with an increase in the Al content, and finally by a slight strengthening (the $Al_{2.5}(NbTiZr)_{97.5}$ and $Al_5(NbTiZr)_{95}$ alloys) or a continuous softening (the $Al_{7.5}(NbTiZr)_{92.5}$ alloy) stage (Figure 3(a)). Similar engineering stress–strain curves with plateau were previously reported in alloys with the bcc (or weakly B2 ordered) structure [46,47,61–63] or in nanolaminates [64]. Although this behaviour should indicate plastic instability and early necking, Wei et al. [63] claimed rather a high value of homogeneous deformation, which they confirmed by DIC

analysis. Indeed, our DIC analysis, coupled with the true stress–strain curves, showed that the macroscopic plastic deformation delocalised with the Al additions in the $Al_x(NbTiZr)_{100-x}$ alloys (Figures 3(b, c) and Figure S3, Supplementary material). As a result, the uniform elongation enlarged from ∼19% in the NbTiZr alloy to ∼26% in the $Al_{7.5}(NbTiZr)_{92.5}$ alloy (Figure 3(b); Table 1).

An analysis of strain hardening rate, θ, revealed a gradual decrease in θ with the strain increment in the NbTiZr alloy (Figure 3(d)). The Al alloying caused the appearance of a 'hump', i.e. a sharp drop in θ at the onset of plastic deformation and a recovery stage with the evolving strain, terminated at peak values of $\theta \approx$ 1000-1100 MPa. The magnitude of the drop and the extension of the recovery stage increased with the Al additions (Figure 3(d)). Lastly, we found that the Al doping did not change the apparent activation volumes, $V*$, significantly (Table 1); details on the determination of $V*$ were described in Supplementary material and Refs [42,65]. The values of $V*$ obtained fell in the range of 10–100 b^3, which meant the thermally activated dislocation glide by overcoming the Peierls-Nabarro barriers was the rate-controlling mechanism of room-temperature plastic deformation in the $Al_x(NbTiZr)_{100-x}$ alloys [42].

Further, we tried to analyse the reasons of a positive impact of the Al additions on the mechanical performance of the $Al_x(NbTiZr)_{100-x}$ alloys. In terms of the strength, the observed increment in YS, ΔYS, induced by the Al alloying was in an agreement with the ones previously reported for Al-containing RHEAs [11,30,66,67] (Figure 4(a)). The strengthening by Al in the studied $Al_x(NbTiZr)_{100-x}$ alloys appeared to be linear with a strengthening rate of ∼ 33 MPa per 1 at.%, which was close to bcc $Al_x(HfNbTiZr)_{100-x}$ (∼ 34 MPa/at.%; [67]) and bcc/B2 $Al_x(Ti_{40}Zr_{20}Hf_{10}V_{20}Nb_{10})_{100-x}$ (∼ 32 MPa/at.%; [30]) RHEAs, but slightly higher than that of bcc $Al_x(HfNbTaTiZr)_{100-x}$ (∼ 25 MPa/at.%; [66]) alloys (Figure 4(a)).

In some alloys, the Al-induced strength increment was ascribed to solid solution strengthening (SSS) [11,66,67]. Given the linear dependence of the ΔYS on the Al content, only the Suzuki model could describe the SSS in Al-containing RH/MEAs [67]. Since Al did not alter the rate-controlling mechanism of plastic deformation in the $Al_x(NbTiZr)_{100-x}$ alloys (Table 1), we suggested that it increased the athermal component of the YS. Thus, the simplified equation, connected the ΔYS and the Al content, could be applied [67]:

$$\Delta YS = \alpha MG\delta^2 c_{Al} \qquad (1)$$

where α is a material-sensitive parameter; M is the Taylor factor; G is the shear modulus of the NbTiZr alloy; δ is the interaction parameter, included the lattice and shear modulus distortions appeared due to the Al additions; c_{Al} is the Al concentration (Table S1, Supplementary material). Details of calculation and constants used are given in Supplementary material.

The ΔYS values obtained by Equation (1) for the $Al_{2.5}(NbTiZr)_{97.5}$ and $Al_5(NbTiZr)_{95}$ alloys were consistent with the experimental ones (Figure 4(b)); however, a small (∼10 MPa) deviation should be noted in the $Al_5(NbTiZr)_{95}$ alloy. Meanwhile, Equation (1) underestimated the ΔYS in the $Al_{7.5}(NbTiZr)_{92.5}$ alloy significantly. Over 50% (∼130 MPa) of the experimentally observed ΔYS remained unaccounted (Figure 4(b)). This discrepancy could be ascribed to the activation of other strengthening mechanisms. Wang et al. [11] and later Qiao et al. [30] mentioned that the B2 ordering could be responsible for the extra strength increment. Due to similarity of the average grain sizes (Figure 1 and Figure S1, Supplementary material), impurities content (Table S1, Supplementary material), and the absence of secondary phase particles in all the studied alloys, we also assumed that the additional increase in the ΔYS of the $Al_{7.5}(NbTiZr)_{92.5}$ alloy stemmed from the B2 SRO strengthening. Recently, SRO was stated as the main contributor to the strength of (R)H/MEAs [68–71] and LWH/MEAs [50,72]. SRO domains usually act as shearable obstacles, increasing the resistance for a dislocation slip due to the creation of diffuse anti-phase boundaries (DAPBs) when being cut [73]. Certainly, the direct evaluation of the SRO strengthening in the $Al_{7.5}(NbTiZr)_{92.5}$ alloy will be feasible only when the energy of DAPB is available from experimental or, at least, calculated data [54], which are absent to date. Also, in the light of microstructural observations shown next, we can not exclude the possibility of the SRO strengthening in the $Al_{2.5}(NbTiZr)_{97.5}$ and $Al_5(NbTiZr)_{95}$ alloys.

Figure 5 displays fine microstructures formed in the $Al_x(NbTiZr)_{100-x}$ alloys during the tensile tests.

In all the alloys, plastic deformation was dominated by $a/2 <111>$ screw dislocations (Figure S5, Supplementary material) but with a significant difference in their spatial distribution (Figure 5). In the NbTiZr alloy, dislocations were distributed homogeneously (Figure 5(a)). Starting from the $Al_{2.5}(NbTiZr)_{97.5}$ alloy, dislocation motion tended to localise in dislocation bands (DBs; denoted with white dashed lines in Figure 5(b)). Further Al additions intensified this process; however, DBs were mutually intersected, suggesting a developed cross-slip (Figures 5(c, d)). In-between these intersected DBs, we found relatively large cells with a reduced dislocation density.

The localisation of plastic deformation in DBs was previously observed in face-centred cubic (fcc) alloys
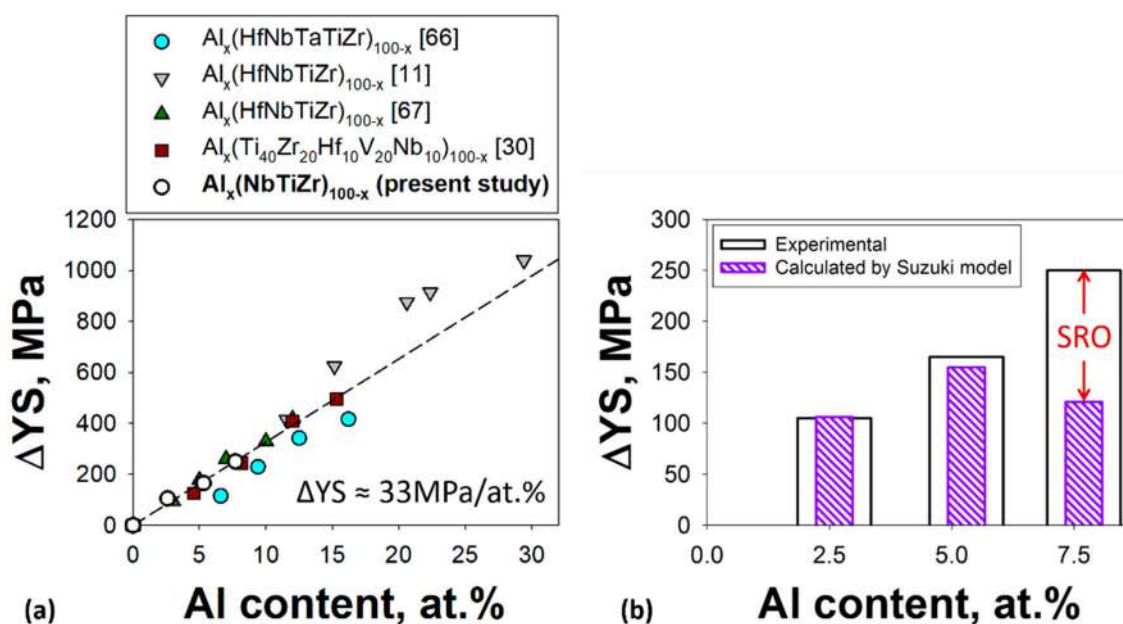
Figure 4. Effect of Al on the strength: (a) a plot, showing the Al-induced increment of YS, $\triangle YS$, in the studied $Al_x(NbTiZr)_{100-x}$ alloys and some other Al-containing RHEAs [11,30,66,67]; (b) a plot, illustrating a comparison between the experimentally observed values of $\triangle YS$ in the $Al_x(NbTiZr)_{100-x}$ alloys and the ones calculated by simplified Suzuki model for SSS. A good correlation for the $Al_{2.5}(NbTiZr)_{97.5}$ and $Al_5(NbTiZr)_{95}$ alloys should be noted. The appeared difference between the experimental and calculated $\triangle YS$ for the $Al_{7.5}(NbTiZr)_{92.5}$ was assumed due to the SRO strengthening (see the text).

[74,75], beta-Ti alloys, Ti-Al-Nb, Ti-rich HEAs, and RHEAs [40,46,47,76–78]. Recent study by Li et al. [75] showed that, in an fcc FeCoCrNiMn alloy, this process could be attributed to heterogeneous lattice strains. Meanwhile, Gerold and Karnthaler [74] demonstrated that localised planar slip in fcc alloys originated from SRO. Zhang et al. [54] further experimentally confirmed a decisive role of SRO domains on the localisation of plastic deformation in the Ti-6Al alloy. Li et al. [76] also connected the formation of DBs in beta-Ti alloys with the presence of SRO domains. Loretto et al. [48] claimed that the emergence of DBs in these alloys was a more solid confirmation of the B2 ordering in alloys with low Al contents compared to SADPs (Figures 1(i-l)). This could mean that even the $Al_{2.5}(NbTiZr)_{97.5}$ alloy had the B2 structure, but the degree of B2 ordering, i.e. the size of B2 SRO domains, was negligible compared to the $Al_5(NbTiZr)_{95}$ and $Al_{7.5}(NbTiZr)_{92.5}$ (Figures 2(b-e)) counterparts.

In terms of the ductility, the localisation of plastic deformation in DBs is considered to be harmful for bcc alloys due to the accumulation of high pile-up stresses, leading to premature fracture [51,69]. Contrastingly, our findings showed that the DBs-proned $Al_{7.5}(NbTiZr)_{92.5}$ alloy achieved a ∼ 37% higher uniform elongation than the NbTiZr alloy with the homogeneous distribution of dislocations (Figure 3; Table 1). It could be connected with changing of strain hardening behaviour. At the onset

of plastic deformation, dislocations in the Al-containing alloys experience higher stresses to motion than in the NbTiZr counterpart due to the presence of the B2 SRO domains. To proceed plastic deformation, dislocations should shear these SRO domains. When it happens, the first dislocations decrease the slip resistance for the following dislocations, resulting in the DBs formation. The latter process is accompanied by the stress reduction and the steep drop of strain hardening rate (Figures 3(a, d); so-called 'glide plane softening' phenomena [74,77]). In turn, plastic deformation within DBs does not eliminate the B2 ordering and only reduces its degree (Figures 5(e-h)), that is, a certain, albeit much reduced, amount of SRO domains persists, similar to results by Zhang et al. [54]. These survived B2 SRO domains seem to create additional (back) stresses, along with the arising contribution of forest hardening [63], for the glide of new dislocations within DBs, thereby leading to the recovery of strain hardening rate (Figure 3(d)). Meantime, the activation of cross-slip results in the formation of new DBs, which help relieve extra pile-up stresses and extend the strengthening stage, thus, delaying necking.

In general, the relative improvement of the mechanical performance of the NbTiZr alloy due to the Al-induced B2 ordering appeared to be more uniform (+ 37% in strength and + 37% in ductility (Table 1)) and, thus, more effective than those of boron (+ 19% in strength and 49% in ductility; [44]) or Mo and Ta (+ 35% in
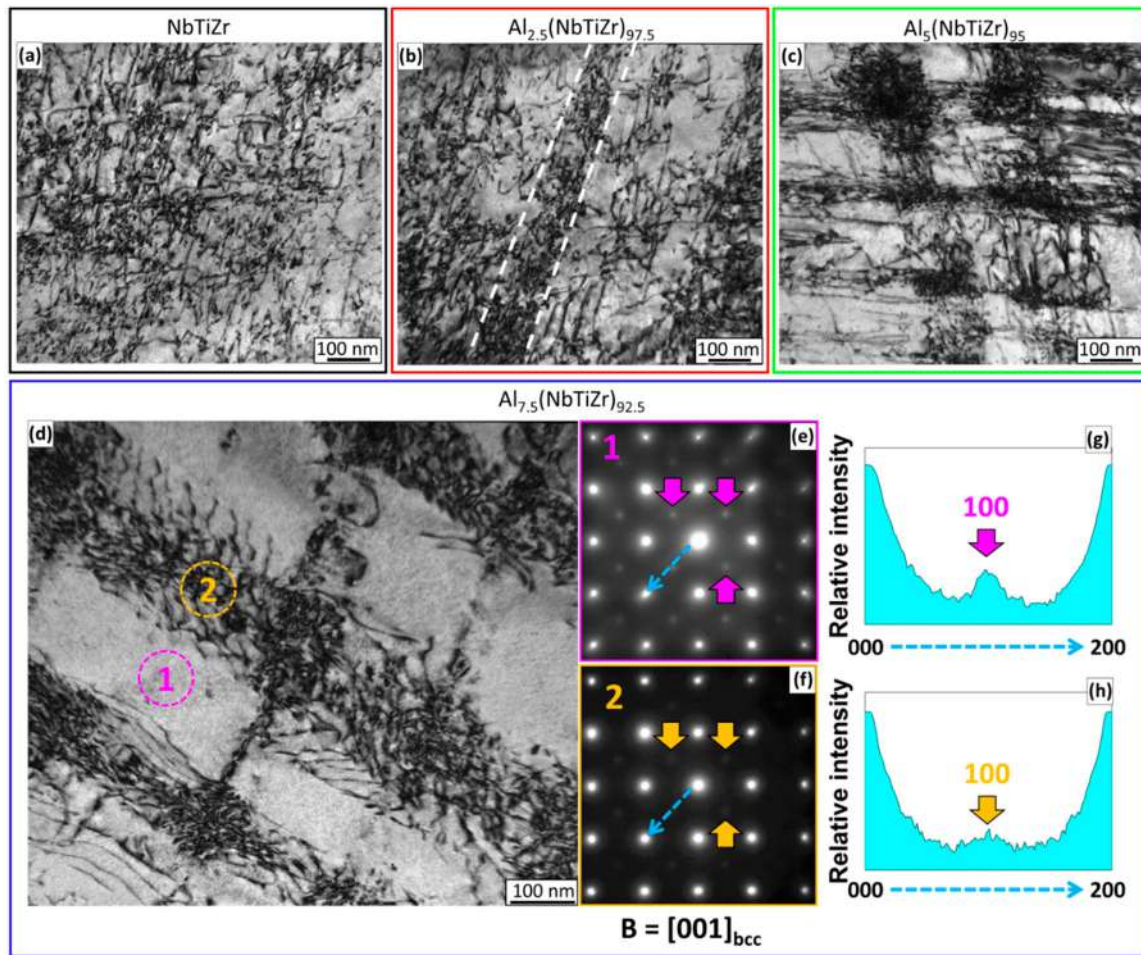
Figure 5. Characterisation of fine microstructure of the $Al_x(NbTiZr)_{100-x}$ alloys after the tensile tests: (a-d) – TEM bright-field images of the dislocation structures, observed in the near-fractured zones of tensile specimens of the NbTiZr (a), $Al_{2.5}(NbTiZr)_{97.5}$ (b), $Al_5(NbTiZr)_{95}$ (c), and $Al_{7.5}(NbTiZr)_{92.5}$ (d) alloys. White dashed lines in Figure 5(d) highlighted the signs of the DBs formation in the $Al_{2.5}(NbTiZr)_{97.5}$ alloy; (e, f) – SADPs taken from cells (denoted as '1' in Figure 5(e)) and DBs (denoted as '2' in Figure 5(f)) in $[001]_{bcc}$ zone axes. Pink and yellow arrows in Figures 5(e, f) denoted the peaks, corresponded to the 100_{B2} superlattice spots in cells and DBs, respectively; (g, h) – intensity line profiles along the g_{200} vectors (the directions are denoted with dashed blue arrows in SADPs Figures 5(e, f)) for the $Al_{7.5}(NbTiZr)_{92.5}$ alloy. Pink and yellow arrows in Figures 5(g, h) denoted the peaks, corresponded to the 100 local maxima in cells and DBs, respectively.

strength and + 16% in ductility; [45]) additions. Naturally, there must be a limit for the Al content, when the B2 ordering deteriorates the mechanical properties of the NbTiZr alloy. We produced an $Al_{15}(NbTiZr)_{85}$ alloy, which was brittle; multiple cracks appeared at early stages of cold rolling (Figure S6, Supplementary material). However, the interval between the $Al_{7.5}(NbTiZr)_{92.5}$ and $Al_{15}(NbTiZr)_{85}$ alloys should be further examined. Also, high-temperature properties and peculiarities of plastic deformation are needed to be investigated. These are goals for future studies.

Conclusions

In summary, we proposed a new strategy to solve the strength-ductility dilemma in RH/MEAs. By invoking

of the B2 ordering and a further controlled increment of its degree during Al alloying, one could enhance the yield strength and uniform elongation from 680 MPa and $\sim$ 19% in the NbTiZr alloy to 930 MPa and $\sim$ 26% in the $Al_{7.5}(NbTiZr)_{92.5}$ alloy. The resulted properties originated from the solid solution and SRO strengthening, as well as from changes in the dislocation glide character. The B2 ordering led to the formation of multiple dislocation bands and the activation of cross-slip, which prolonged the strengthening stage and prevented early necking.

Data availability statement

The data that support the findings of this study are available from the corresponding author upon reasonable request.

Acknowledgements

Disclosure statement

No potential conflict of interest was reported by the author(s).

Funding

ORCID

N. Yurchenko http://orcid.org/0000-0002-6078-8325
E. Panina http://orcid.org/0000-0002-9440-887X
S. Zherebtsov http://orcid.org/0000-0002-1663-429X
N. Stepanov http://orcid.org/0000-0003-2476-3953

References

[1] Senkov ON, Wilks GB, Miracle DB, et al. Refractory high-entropy alloys. Intermetallics. 2010;18:1758–1765.

[2] Miracle DB, Senkov ON. A critical review of high entropy alloys and related concepts. Acta Mater. 2017;122:448–511.

[3] Senkov ON, Miracle DB, Chaput KJ, et al. Development and exploration of refractory high entropy alloys - a review. J Mater Res. 2018;33:3092–3128.

[4] Senkov ON, Gorsse S, Miracle DB. High temperature strength of refractory complex concentrated alloys. Acta Mater. 2019;175:394–405.

[5] Jensen JK, Welk BA, Williams REA, et al. Characterization of the microstructure of the compositionally complex alloy $Al_1Mo_{0.5}Nb_1Ta_{0.5}Ti_1Zr_1$. Scr Mater. 2016;121:1–4.

[6] Senkov ON, Isheim D, Seidman DN, et al. Development of a refractory high entropy superalloy. Entropy. 2016;18:1–13.

[7] Yurchenko NY, Stepanov ND, Zherebtsov S V, et al. Structure and mechanical properties of B2 ordered refractory $AlNbTiVZr_x$ (x = 0–1.5) high-entropy alloys. Mater Sci Eng A. 2017;704:82–90.

[8] Stepanov ND, Yurchenko NY, Gridneva AO, et al. Structure and hardness of B2 ordered refractory $AlNbTiVZr_{0.5}$ high entropy alloy after high-pressure torsion. Mater Sci Eng A. 2018;716:308–315.

[9] Senkov ON, Jensen JK, Pilchak AL, et al. Compositional variation effects on the microstructure and properties of a refractory high-entropy superalloy $AlMo_{0.5}NbTa_{0.5}TiZr$. Mater Des. 2018;139:498–511.

[10] Soni V, Senkov ON, Gwalani B, et al. Microstructural design for improving ductility of an initially brittle refractory high entropy alloy. Sci Rep. 2018: 1–10.

[11] Wang W, Zhang Z, Niu J, et al. Effect of Al addition on structural evolution and mechanical properties of the $Al_xHfNbTiZr$ high-entropy alloys. Mater Today Commun. 2018;16:242–249.

[12] Soni V, Gwalani B, Senkov ON, et al. Phase stability as a function of temperature in a refractory high-entropy alloy. J Mater Res. 2018;33:3235–3246.

[13] Yurchenko NY, Stepanov ND, Gridneva AO, et al. Effect of Cr and Zr on phase stability of refractory Al-Cr-Nb-Ti-V-Zr high-entropy alloys. J Alloys Compd. 2018;757:403–414.

[14] Chen H, Kauffmann A, Seils S, et al. Crystallographic ordering in a series of Al-containing refractory high entropy alloys Ta–Nb–Mo–Cr–Ti–Al. Acta Mater. 2019; 176:123–133.

[15] Schliephake D, Medvedev AE, Imran MK, et al. Precipitation behaviour and mechanical properties of a novel $Al_{0.5}MoTaTi$ complex concentrated alloy. Scr Mater. 2019;173:16–20.

[16] Yurchenko N, Panina E, Tikhonovsky M, et al. Structure and mechanical properties of an in situ refractory $Al_{20}Cr_{10}Nb_{15}Ti_{20}V_{25}Zr_{10}$ high entropy alloy composite. Mater Lett. 2020;264:127372.

[17] Soni V, Senkov ON, Couzinie J-P, et al. Phase stability and microstructure evolution in a ductile refractory high entropy alloy $Al_{10}Nb_{15}Ta_5Ti_{30}Zr_{40}$. Materialia [Internet]. 2020;9:100569.

[18] Soni V, Gwalani B, Alam T, et al. Phase inversion in a two-phase, BCC + B2, refractory high entropy alloy. Acta Mater. 2020;185:89–97.

[19] Laube S, Chen H, Kauffmann A, et al. Controlling crystallographic ordering in Mo–Cr–Ti–Al high entropy alloys to enhance ductility. J Alloys Compd. 2020;823:153805.

[20] Müller F, Gorr B, Christ H-J, et al. Formation of complex intermetallic phases in novel refractory high-entropy alloys NbMoCrTiAl and TaMoCrTiAl: thermodynamic assessment and experimental validation. J Alloys Compd. 2020: 155726.

[21] Yurchenko N, Panina E, Tikhonovsky M, et al. A new refractory Ti-Nb-Hf-Al high entropy alloy strengthened by orthorhombic phase particles. Int J Refract Met Hard Mater. 2020;92:105322.

[22] Whitfield TE, Pickering EJ, Owen LR, et al. The effect of Al on the formation and stability of a BCC – B2 microstructure in a refractory metal high entropy superalloy system. Materialia. 2020;13:100858.

[23] Miracle DB, Tsai MH, Senkov ON, et al. Refractory high entropy superalloys (RSAs). Scr Mater. 2020;187:445–452.

[24] Senkov ON, Couzinie J-P, Rao SI, et al. Temperature dependent deformation behavior and strengthening mechanisms in a low density refractory high entropy alloy $Al_{10}Nb_{15}Ta_5Ti_{30}Zr_{40}$. Materialia. 2020;9:100627.

[25] Kral P, Blum W, Dvorak J, et al. Creep behavior of an $AlTiVNbZr_{0.25}$ high entropy alloy at 1073 K. Mater Sci Eng A. 2020;783:139291.

[26] Wang Q, Han J, Liu Y, et al. Coherent precipitation and stability of cuboidal nanoparticles in body-centered-cubic $Al_{0.4}Nb_{0.5}Ta_{0.5}TiZr_{0.8}$ refractory high entropy alloy. Scr Mater. 2021;190:40–45.

[27] Yurchenko N, Panina E, Zherebtsov S, et al. Design and characterization of eutectic refractory high entropy alloys. Materialia. 2021;16:101057.

[28] Panina E, Yurchenko N, Zherebtsov S, et al. Aging behavior of two refractory Ti-Nb-(Hf. Zr)-Al high entropy alloys. J Alloys Compd. 2021;889:161586.

[29] Liu XW, Bai ZC, Ding XF, et al. A novel light-weight refractory high-entropy alloy with high specific strength and intrinsic deformability. Mater Lett. 2021;287:129255.

[30] Qiao D, Liang H, Wu S, et al. The mechanical and oxidation properties of novel B2-ordered $Ti_2ZrHf_{0.5}VNb_{0.5}Al_x$ refractory high-entropy alloys. Mater Charact. 2021;178:111287.

[31] Laube S, Schellert S, Tirunilai AS, et al. Microstructure tailoring of Al-containing compositionally complex alloys by controlling the sequence of precipitation and ordering. Acta Mater. 2021;218:117217.

[32] Yurchenko NY, Panina ES, Salishchev GA, et al. Design and characterization of Al-Cr-Nb-Ti-V-Zr high-entropy alloys for high-temperature applications. Phys Mesomech. 2021;24:642–652.

[33] Yang X, An Z, Zhai Y, et al. Effect of Al content on the thermal oxidation behaviour of AlHfMoNbTi high-entropy alloys analysed by in situ environmental TEM. Corros Sci. 2021;191:109711.

[34] Wang Z, Jin D, Han J, et al. Microstructures and mechanical properties of Al-Ti-Zr-Nb-Ta-Mo-V refractory high-entropy alloys with coherent B2 nanoprecipitation. Cryst. 2021;11:833.

[35] Dong Y-G, Chen S, Jia N-N, et al. Microstructures and mechanical properties of Ta–Nb–Zr–Ti–Al refractory high entropy alloys with varying Ta/Ti ratios. Tungsten. 2021;3:406–414.

[36] Pang J, Zhang H, Zhang L, et al. A ductile $Nb_{40}Ti_{25}Al_{15}V_{10}Ta_5Hf_3W_2$ refractory high entropy alloy with high specific strength for high-temperature applications. Mater Sci Eng A. 2022;831:142290.

[37] Yurchenko N, Panina E, Belyakov A, et al. On the yield stress anomaly in a B2-ordered refractory AlNbTiVZr0.25 high-entropy alloy. Mater Lett. 2022;311:131584.

[38] Zhao B, Chen G, Lv S, et al. A refractory multi-principal element alloy with superior elevated-temperature strength. J Alloys Compd. 2022;896:163129.

[39] Dasari S, Soni V, Sharma A, et al. Concomitant clustering and ordering leading to B2 + BCC microstructures in refractory high entropy alloys. Trans Indian Inst Met. 2022;75:907–916.

[40] Couzinié J-P, Heczko M, Mazánová V, et al. High-temperature deformation mechanisms in a BCC + B2 refractory complex concentrated alloy. Acta Mater. 2022;233:117995.

[41] Senkov ON, Miracle DB, Rao SI. Correlations to improve room temperature ductility of refractory complex concentrated alloys. Mater Sci Eng A. 2021;820:141512.

[42] Eleti RR, Stepanov N, Yurchenko N, et al. Plastic deformation of solid-solution strengthened Hf-Nb-Ta-Ti-Zr body-centered cubic medium/high-entropy alloys. Scr Mater. 2021;200:113927.

[43] Eleti RR, Stepanov N, Yurchenko N, et al. Cross-kink unpinning controls the medium- to high-temperature strength of body-centered cubic NbTiZr medium-entropy alloy. Scr Mater. 2022;209:114367.

[44] Pang J, Zhang H, Zhang L, et al. Simultaneous enhancement of strength and ductility of body-centered cubic TiZrNb multi-principal element alloys via boron-doping. J Mater Sci Technol. 2021;78:74–80.

[45] Akmal M, Seong HW, Ryu HJ. Mo and Ta addition in NbTiZr medium entropy alloy to overcome tensile yield strength-ductility trade-off. J Mater Sci Technol. 2022;109:176–185.

[46] Zherebtsov S, Yurchenko N, Panina E, et al. Gum-like mechanical behavior of a partially ordered $Al_5Nb_{24}Ti_{40}V_5Zr_{26}$ high entropy alloy. Intermetallics. 2020;116:106652.

[47] Zherebtsov S, Yurchenko N, Panina E, et al. Microband-induced plasticity in a Ti-rich high-entropy alloy. J Alloys Compd. 2020;842:155868.

[48] Loretto MH, Hu D, Li YG. Microstructural studies on some ordered Ti-based alloys. Intermetallics. 2000;8:1243–1249.

[49] Liao YC, Ye WT, Chen PS, et al. Effect of Al concentration on the microstructural and mechanical properties of lightweight $Ti_{60}Al_x(VCrNb)_{40-x}$ medium-entropy alloys. Intermetallics. 2021;135:107213.

[50] Wang L, Chen S, Li B, et al. Lightweight Zr1.2V0.8 NbTixAly high-entropy alloys with high tensile strength and ductility. Mater Sci Eng A. 2021;814:141234.

[51] Li YG, Blenkinsop PA, Loretto MH, et al. Effect of aluminium on ordering of highly stabilised β-Ti-V-Cr alloys. Mater Sci Technol. 1998;14:732–737.

[52] Yang KH, Choo WK. Evidence of carbon ordering and morphology change in a cubic carbide phase. Philos Mag Lett. 1990;62:221–226.

[53] Kim SD, Park JY, Park SJ, et al. Direct observation of dislocation plasticity in high-Mn lightweight steel by in-situ TEM. Sci Rep. 2019;9:1–13.

[54] Zhang R, Zhao S, Ophus C, et al. Direct imaging of short-range order and its impact on deformation in Ti-6Al. Sci Adv. 2019;5:eaax2799.

[55] Chong Y, Zhang R, Hooshmand MS, et al. Elimination of oxygen sensitivity in α-titanium by substitutional alloying with Al. Nat Commun. 2021;12:1–9.

[56] Miao J, Slone C, Dasari S, et al. Ordering effects on deformation substructures and strain hardening behavior of a CrCoNi based medium entropy alloy. Acta Mater. 2021;210:116829.

[57] Dasari S, Jagetia A, Sharma A, et al. Tuning the degree of chemical ordering in the solid solution of a complex concentrated alloy and its impact on mechanical properties. Acta Mater. 2021;212:116938.

[58] Passa E, Shao G, Tsakiropoulos P. Beta phase decomposition in Nb-17 at.% Al alloy. Philos Mag A Phys Condens Matter. Struct Defects Mech Prop. 1997;75:637–655.

[59] Chen X, Wang Q, Cheng Z, et al. Direct observation of chemical short-range order in a medium-entropy alloy. Nat. 2021;592:712–716.

[60] Wang J, Jiang P, Yuan F, et al. Chemical medium-range order in a medium-entropy alloy. Nat Commun. 2022;131:1–6.

[61] Saito T, Furuta T, Hwang J-H, et al. Multifunctional alloys obtained via a dislocation-free plastic deformation mechanism. Science. 2003;300:464–467.

[62] Lai MJ, Tasan CC, Raabe D. Deformation mechanism of ω-enriched Ti–Nb-based gum metal: dislocation

channeling and deformation induced ω–β transformation. Acta Mater. 2015;100:290–300.

[63] Wei S, Kim SJ, Kang J, et al. Natural-mixing guided design of refractory high-entropy alloys with as-cast tensile ductility. Nat Mater 2020 1911. 2020;19:1175–1181.

[64] Wang Y, Li J, Hamza A V, et al. Ductile crystalline-amorphous nanolaminates. Proc Natl Acad Sci U S A. 2007;104:11155–11160.

[65] Eleti RR, Stepanov N, Zherebtsov S. Mechanical behavior and thermal activation analysis of HfNbTaTiZr body-centered cubic high-entropy alloy during tensile deformation at 77 K. Scr Mater. 2020;188:118–123.

[66] Lin C-M, Juan C-C, Chang C-H, et al. Effect of Al addition on mechanical properties and microstructure of refractory Al_xHfNbTaTiZr alloys. J Alloys Compd. 2015;624:100–107.

[67] Wu Y, Si J, Lin D, et al. Phase stability and mechanical properties of AlHfNbTiZr high-entropy alloys. Mater Sci Eng A. 2018;724:249–259.

[68] Maiti S, Steurer W. Structural-disorder and its effect on mechanical properties in single-phase TaNbHfZr high-entropy alloy. Acta Mater. 2016;106:87–97.

[69] Lei Z, Liu X, Wu Y, et al. Enhanced strength and ductility in a high-entropy alloy via ordered oxygen complexes. Nature. 2018;563:546–550.

[70] Li Q-J, Sheng H, Ma E. Strengthening in multi-principal element alloys with local-chemical-order roughened dislocation pathways. Nat Commun. 2019;10:3563.

[71] Schön CG. On short-range order strengthening and its role in high-entropy alloys. Scr Mater. 2021;196:113754.

[72] Pang J, Zhang H, Zhang L, et al. Ductile $Ti_{1.5}$ZrNbAl$_{0.3}$ refractory high entropy alloy with high specific strength. Mater Lett. 2021;290:129428.

[73] Fisher JC. On the strength of solid solution alloys. Acta Metall. 1954;2:9–10.

[74] Gerold V, Karnthaler HP. On the origin of planar slip in f.c.c. alloys. Acta Metall. 1989;37:2177–2183.

[75] Li J, Chen Y, He Q, et al. Heterogeneous lattice strain strengthening in severely distorted crystalline solids. Proc Natl Acad Sci. 2022;119:1–7.

[76] Li YG, Blenkinsop PA, Loretto MH, et al. Effect of aluminium on deformation structure of highly stabilised beta-Ti-V-Cr alloys. Mater Sci Technol. 1999;15:151–155.

[77] Banerjee D, Gogia AK, Nandy TK. Deformation structure in a Ti-24Al-11Nb alloy. Metall Trans A. 1990;21:627–639.

[78] Lilensten L, Couzinié J-P, Perrière L, et al. Study of a bcc multi-principal element alloy: tensile and simple shear properties and underlying deformation mechanisms. Acta Mater. 2018;142:131–141.